Minimagnetospheres above the Lunar Surface and the Formation of Lunar Swirls

R. A. Bamford,[1,*] B. Kellett,[1] W. J. Bradford,[1] C. Norberg,[2] A. Thornton,[3] K. J. Gibson,[3] I. A. Crawford,[4] L. Silva,[5] L. Gargaté,[5] and R. Bingham[6,†]

[1]*RAL Space, Rutherford Appleton Laboratory, Chilton, Didcot, OX11 0QX, United Kingdom*
[2]*Swedish Institute of Space Physics, Box 812, SE-981 28 Kiruna, Sweden*
[3]*York Plasma Institute, Department of Physics, University of York, Heslington, York, YO10 5DD, United Kingdom*
[4]*Department of Earth and Planetary Sciences, Birkbeck College, London, United Kingdom*
[5]*Instituto Superior Técnico, 1049-00, Lisboa, Portugal*
[6]*University of Strathclyde, Glasgow, Scotland, United Kingdom*

(Received 28 April 2012; published 20 August 2012; publisher error corrected 24 August 2012)

In this paper we present *in situ* satellite data, theory, and laboratory validation that show how small-scale collisionless shocks and minimagnetospheres can form on the electron inertial scale length. The resulting retardation and deflection of the solar wind ions could be responsible for the unusual ''lunar swirl'' patterns seen on the surface of the Moon.

DOI: 10.1103/PhysRevLett.109.081101 PACS numbers: 52.72.+v, 52.35.Tc, 94.05.−a, 96.20.Jz

Miniature magnetospheres have been found to exist above the lunar surface [1] and are closely related to features known as ''lunar swirls'' [2]. Minimagnetospheres exhibit features that are characteristic of normal planetary magnetospheres, namely, a collisionless shock. Here we show that it is the electric field associated with the small-scale collisionless shock that is responsible for deflecting the incoming solar wind around the minimagnetosphere. Solar wind ions impacting the lunar surface result in changes to the appearance of the albedo of the lunar ''soil''[2]. The form of these swirl patterns therefore must be dictated by the shapes of the collisionless shock.

Collisionless shocks are a classic phenomenon in plasma physics, ubiquitous in many space and astrophysical scenarios [3]. Well-known examples of collisionless shocks exist in the heliosphere, where the shock is formed by the solar wind interacting with a magnetized planet. What is a surprise is the size of the minimagnetospheres, of the order of several 100 km, orders of magnitude smaller than the planetary versions. Results from various lunar survey missions have built up a good picture of these collisionless shocks.

These collisionless shocks have a characteristic structure in which the ions are reflected from a rather narrow layer, of the order of the electron skin depth c/ω_{pe} (where c is the speed of light and ω_{pe} is the electron plasma frequency). An electrostatic field arises as a consequence of the magnetized electrons and unmagnetized ions. The narrow discontinuity in the shock structure produces a specular reflected ion component with a velocity equal to or greater than the incoming solar wind velocity. The reflected ions form a counterpropagating component to the solar wind flow creating the magnetic foot region, which extends about an ion Larmor orbit upstream from the shock. This occurs when the Mach number (the ratio of flow velocity to Alfvén velocity) is of the order 3 or less.

We have carried out laboratory experiments using a plasma wind tunnel, to investigate minimagnetospheres and found that they show characteristics similar to the lunar minimagnetospheres. A quantified comparison between the observations, both in space and in the laboratory, with theoretical values shows excellent agreement.

The Reiner Gamma Formation shown in Fig. 1 is one example of a number of small swirls of apparently lighter colored material visible on the lunar surface. These distinctive patterns do not appear to correlate with other surface features, such as impact craters or mountains and valleys, but do coincide with patches of significant magnetic field [2]. All of these lunar swirls have been found to be associated with magnetic anomalies [2]. The appearance of lighter albedo material on the Moon is usually indicative of the presence of younger or less

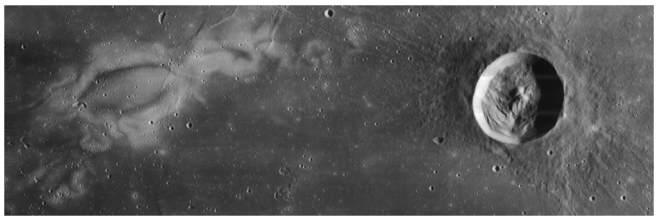

FIG. 1. The Reiner Gamma formation (7.4°N, 300.9°E) is an example of a lunar swirl. Pictured here on the left-hand side of the image. Reiner Gamma is named after the Reiner impact crater shown for comparison on the right. The crater is 117 km to the east and has diameter of 30 km with a depth of 2.6 km. By contrast, the unusual diffuse swirling of the formation and concentric oval shape has fluidlike wisps that extend further to the east and west. Its distinctive lighter color stands out against the flat, dark surface of Oceanus Procellarum. Unlike crater ejecta, the shape of the formation appears unrelated to any topographic structures that would account for its presence. Image courtesy of NASA.

weathered lunar material [4]. Explanations that account for these changes in the albedo are either (a) that the lighter regions have been shielded from receiving the same solar wind flux as the surrounding regolith and hence appear younger [2], or (b) that the lighter color material originates from just below the surface and has been lifted up and deposited on the top of older or darker regolith [5]. The sharpness of the lunar swirl formations is enhanced by the contrast of "dark lanes" (suggesting locally enhanced solar wind proton bombardment) within the high-albedo swirls.

In situ measurements from spacecraft, including Lunar Prospector (1998–1999) [6], Kaguya (2007–2009) [7], Chandrayaan-1 (2008–2009) [8], and Nozomi (1998) spacecraft [9], are consistent with the presence of collisionless shocks and the formation of minimagnetospheres. Because the observational data derive from a sequence of case studies from different missions [1,10–16], it is to be expected that there is some variation in consistency. However a schematic picture of the interaction can be unraveled from the specific observations to form a simplified, generic model. This is illustrated in Fig. 2.

A region of enhanced magnetic field strength (by factors of 2 to 3) is observed at an altitude x_s above the lunar surface where the magnetic intensity from the magnetic anomaly reaches pressure balance with the plasma pressure from the solar wind. The magnetic field components were observed to rotate in a fashion consistent with the spacecraft passing through a region in which the solar magnetic field was being "draped" around a small magnetic obstacle or "bubble" [1]. Within the narrow barrier region is a low-density cavity seen in the ion data [17]. The barrier region is of the order of kilometers across. Just ahead of a large ramp in magnetic field strength there is enhanced magnetic field turbulence in the solar wind magnetic field [1]. This is accompanied by electrostatic solitary waves at the lower hybrid frequency and electron fluxes abruptly increase and their energy distribution changes, indicating that electrons

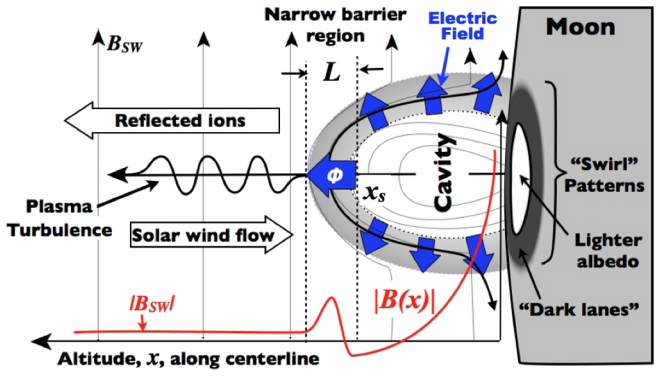

FIG. 2 (color online). A sketch of the generic scenario of a miniature magnetic field emerging from the lunar surface and interacting with the solar wind. Flow is from left to right.

are energized and not simply compressed [1,10–13,15]. Intense electrostatic waves, of frequencies of the order of the plasma lower hybrid frequencies (1–10 Hz), were recorded over the locations of the magnetic anomalies by the Kaguya spacecraft [12,13]. Variations in the intensity of these waves over magnetic anomalies with solar wind pressure suggests a dynamic interaction [12]. At 100 km, Kaguya observed protons reflected back from the magnetic structures with greater energies (by factors 3 to 6) than the incident solar wind flux [13]. Chandrayaan-1 also observed backstreaming protons accelerated by similar factors close to the shock surface [11,17]. These higher energy protons are accelerated by the convective electric field seen by the reflected protons in the solar wind flow [13]. Below 50 km altitude, proton backscattering disappeared [14], indicating that the flowing solar wind ions were no longer reaching these altitudes, and suggesting that the spacecraft was flying through a solar wind plasma "cavity." Chandrayaan-1 provided two-dimensional maps of the spatial extent of the cavity above the magnetic anomaly near the Gerasimovic crater [11]. The dimensions of the cavity and the magnetic field anomaly ($\sim$ 360 km across) were very similar. The cavity was more distinct in the higher energy ions $>$150 eV than at lower energies. The overall size was about 360 km in diameter, coincident with the center of the magnetic anomaly. An outer ring (about 300 km wide) of enhanced proton flux suggested that the incoming solar wind ions were being deflected around from the central bubble to impact the surface in this relatively narrow surrounding region. Observations provided by the Nozomi spacecraft in 1998 suggest that characteristic wakes arising from the lunar minimagnetospheres can extend to significant altitudes (2800 km). The instrumentation onboard recorded two peaks in nonthermal proton density on either side of a cavity of reduced ion flux [16]. These observations agree with those of Chandrayaan-1 at intermediate altitudes above the minimagnetosphere bow shock [15].

The key to understanding how such structures can arise is to use a two-fluid model of the plasma, in which the ions in the flowing plasma are unmagnetized and the electrons are magnetized. As the solar wind with its embedded magnetic field impacts a magnetic structure, a cavity is created. The cavity is bounded by an enhanced magnetic field that is about a factor three greater than the solar wind field with a width, L, estimated to be similar to the electron skin depth. This field traps a low-density plasma that forms part of the barrier. The cavity is created by the induced currents that flow on its outer boundary, giving rise to magnetic field enhancement that opposes the penetration of the solar wind, according to Lenz's law. The enhanced magnetic field drapes around the cavity.

The magnetic field enhancement shown in the satellite observations controls the flow of the electrons that are magnetized on these scales. The solar wind electrons are

slowed and deflected by the magnetic structure. The ions, on the other hand, due to their greater inertia, cannot respond sufficiently promptly to abrupt or sudden changes in magnetic field on these scales. These unmagnetized ions can therefore easily penetrate through the barrier. Ions flowing through the barrier result in a space charge separation between the electrons and ions, forming an electric field that is responsible for slowing and reflecting or deflecting of the ions over distances of the order of the electron skin depth [18].

The equation of motion that controls the behavior of the ions is [19]

$$n_i \frac{d}{dx}\left(\frac{1}{2} m_i v_i^2 + e\phi\right) + \frac{dp_i}{dx} = 0, \tag{1}$$

where ϕ is the electric potential ramp across the barrier, the ion pressure $p_i = n_i k T_i$, and v_i is the ion velocity, the bulk value of which is the solar wind speed, $\sim v_{\rm sw}$.

The expression for the electric potential component, ϕ, responsible for slowing and deflecting the ions is [20,21]

$$\phi = -\frac{1}{2\mu_0 ne} B_z^2. \tag{2}$$

If the instantaneous density, n, here is $\sim 5 \times 10^6$ m^{-3} and a magnetic field $B_z \sim 30 \times 10^{-9} T$, values similar to those observed at the pileup reported by Lunar Prospector [1], then the mean value from (2) of the potential would be $\phi_{\rm theory} \sim 450$ V. This average value is very similar to the $\phi_{\rm obs} \sim 400$ V [15] and would account for the observed counterstreaming protons. Although the force does act initially on the electrons, the resulting electric field formed then acts on the ions. The consequence is that this force acts to keep particles out of regions of high magnetic field. The shock thickness of the electric field, L, is much narrower than the ion Larmor radius. The ions experience a sufficient impulsive force in a direction normal to the barrier to reverse their velocity. These ions move upstream with a velocity $2v_{\rm sw}$ in the solar wind frame and form a broad, much thicker region than the barrier, sometimes known as the shock foot. Within the shock foot region, the counterstreaming ions are responsible for a number of microinstabilities, such as the modified two-stream instability [22] that drives plasma wave turbulence close to the lower hybrid frequency $= (\omega_{\rm ce}\omega_{\rm ci})^{1/2}$, where $\omega_{\rm ce}$ and $\omega_{\rm ci}$ are the electron and ion cyclotron frequencies, respectfully. This would agree with data from all the spacecraft that observed intense lower-hybrid electrostatic oscillations of the order of 1–10 Hz [16]. The reflected or deflected ions can also form a nonthermal ring distribution in ion velocity space due to $E \times B$ pickup, exactly as reported [16]. Alternatively a simple counterstreaming population would be observed, depending on the particular conditions intersected by the spacecraft on its fly-through. Both are consistent. The changes in the particle distributions observed by the *in situ* spacecraft, between the ions and electrons on either side of the shock, result from the formation and interaction of lower-hybrid waves generated close to the bow shock [23]. The resonant interaction between lower-hybrid turbulence and electrons can result in field-aligned electron acceleration [23]. These waves are most probably excited by the modified two-stream instability driven by reflected ions.

The density of transformed electrons, $n_{\rm Te}$, is estimated by balancing the growth rate of the instability initiated by pickup ions with Landau damping due to electrons moving parallel to the magnetic field. Estimations for the average energy, ϵ_e, of the accelerated electrons and their number density $n_{\rm Te}$ can be made [23]:

$$\epsilon_e \approx \alpha^{2/5}\left(\frac{m_e}{m_i}\right)^{1/5} m_i v_{\rm sw}^2, \tag{3}$$

$$n_{Te} \approx n_i \alpha^{2/5}\left(\frac{m_e}{m_i}\right)^{1/5}, \tag{4}$$

where α is the energy transformation efficiency from ions to electrons (with masses m_i and m_e, respectfully).

The energy transformation coefficient, α, has only a weak influence on the result [23]. Therefore using a value of $\alpha \sim 0.1$, the case near a bow shock, with an ion energy of ~ 1 keV and electron energy $\epsilon_e \sim 100$ eV, the density of the accelerated electrons would be 10% of the ion density ($n_{\rm Te} \simeq 0.1 n_i$). This is consistent with the typical values reported by Kaguya [14] and Chandrayaan-1 [24]. This simple estimate demonstrates the large efficiency of lower-hybrid waves as an acceleration mechanism for the electrons. The result is a more efficient boundary than would be predicted by magnetohydrodynamics; comparisons with the particle distribution data could confirm this. The theoretical width of the barrier is expected to be of the order of the electron skin depth, $L = 1$ to 2 km, and not the hundreds of kilometers of the ion skin depth [18]. See Table I for typical values.

Computational simulations of kinetic processes are nontrivial. A scaled laboratory experiment has the potential to deliver physical insights and to offer observational signatures which can be examined, to establish whether or not they are consistent with the *in situ* space data. The Plasma Wind Tunnel [25] used here shares the same phenomenological regime as the subset of analogous space parameters. These are: the plasma is collisionless, the bulk flow speed is supersonic, and the electrons are magnetized but the ions are not. The absolute and dimensionless parameters are given in Table I.

In Fig. 3 we show two photographs of the Plasma Wind Tunnel in action. The supersonic hydrogen plasma stream is here impacting the magnetic dipole fields of two different-sized magnets under the same conditions. The plasma stream appears dark on the photograph and is enhanced for clarity. The structures are three-dimensional so some blurring due to line-of-sight occurs. Despite the

TABLE I. A comparison of the absolute and dimensionless (Dim') distances (normalized to c/ω_{pi}), in space and the laboratory experiment.

	Space		Laboratory	
Parameter in SI units	Value	Dim'	Value	Dim'
Thermal energy, eV	5		5	
Density, m^{-3}	5×10^6		10^{17}	
Flow speed, ms^{-1}	4×10^5		8×10^4	
Magnetic field strength, T	10^{-8}		0.03	
Plasma beta	0.1		2×10^{-4}	
Mach number, acoustic, Alfvénic	20, 5		3.5, 0.03	
Flow mean free path, m	10^{16}	10^{11}	300	400
Debye length, m	7	10^{-5}	5×10^{-5}	7×10^{-5}
Electron Larmor radius, m	800	8×10^{-3}	3×10^{-4}	4×10^{-4}
Thermal ion Larmor radius, m	6×10^4	0.6	10^{-2}	0.01
Flow ion Larmor radius, m	5×10^5	5	3×10^{-2}	0.04
Electron skin depth, m	2×10^3	0.02	2×10^{-3}	0.01
Ion skin depth c/ω_{pi}, m	10^5	1	0.7	1

greater than 2× difference in the size of the magnetic bubble obstacle in the two cases, the plasma stream is corralled the same way into a narrow boundary layer and deflected around the outsides to form a cavity. The key inset shows the ion Larmor radius to scale with the photographic data, demonstrating that the interaction is on the subion Larmor radius scale as with the lunar case.

The Langmuir probe data shown in Fig. 4 correspond to the larger of the two magnets shown in Fig. 3. The ion density shown in the upper panel confirms the formation of a cavity or void in the plasma stream. The floating electric potential (lower panel) coincides with the locations of the measured ion density shown in the upper panel. This demonstrates that the ions are indeed electrostatically confined on this scale. The measured width of the boundary layer is between 2 and 3 mm, similar to the calculated electron skin depth of ~2 mm [18] and is very much less than the calculated ion inertial length of 700 mm or the 30 mm of the ion Larmor radius (see Table I). The quantified relation between the ion density and the electric potential can be better compared in the one-dimensional plot shown in Fig. 5. At the point x_s shown in the figure, the measured electric potential is $\phi_{\text{obs}} \sim 8$ V. Here again, the estimate provided by Eq. (2) provides a good match to the observed value with $\phi_{\text{theory}} \sim 12.5$ V (using $B = 0.05$ T, $n = 5 \times 10^{16}$ m^{-3}). This shows that the dimensionless analysis holds on a very different absolute scale to the case in space.

The analysis presented here shows that the strength of the deflecting electric field of a minimagnetosphere and collisionless shock is not dependent on the overall size of the magnetic bubble but is related to the local *gradient* in the magnetic field strength. None of the real features are simple single dipoles. Close to the surface, the magnetic topology in a magnetic anomaly is likely to be very irregular, comprising a range of overlapping cavities and gradients. This would lead to a pattern of retarded and

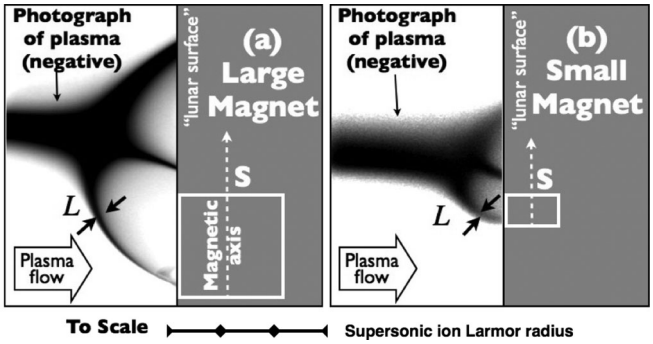

FIG. 3. Photographs, with graphical labels overlaid, of the supersonic plasma stream being deflected by two different-strength magnets. (a) 23 × 20 mm, 0.45 T on axis. (b) 10 × 3 mm, 0.30 T on axis. External horizontal magnetic field is 0.03 T. A field-aligned current can be seen connecting the cusp region to the southern poles in both cases.

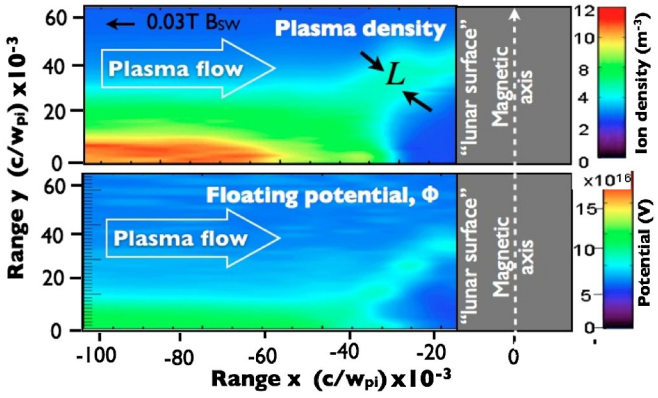

FIG. 4 (color online). *In situ* Langmuir probe plots of the plasma density and floating potential ahead of the larger target magnet (23 × 20 mm, 0.45 T). Data from Ref. [26].

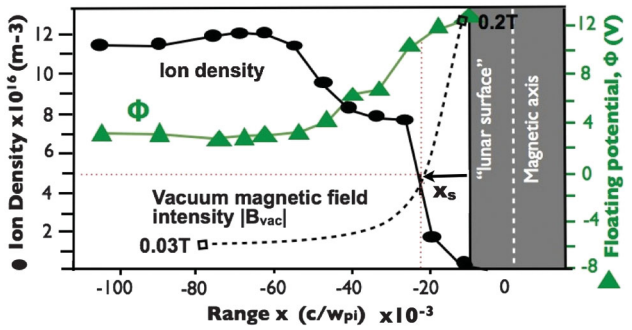

FIG. 5 (color). A plot of the measured ion density (black dots) and electric potential (green triangles) along the axis of the experiment in the vertical plane. The plasma flow is from left to right. Data from Ref. [26].

accelerated space weathering and hence areas of lighter material with embedded dark lanes. A further range of contrasts in the surface aging would come from the variations in the impacting plasma wind environment with solar activity, the Moon's orbit in and out of the Earth's magnetosphere, and lunar phases.

In conclusion, the model of small-scale collisionless shocks that we present agrees with a laboratory plasma wind tunnel experiment confirming the presence of a narrow electrostatic potential of thickness of the order of the local electron skin depth, and that it is the force responsible for the control and deflection of the ions. All the observational data from spacecraft are quantifiably consistent with the theoretical model.

The authors would like to thank Science and Technology Facilities Research Council's Center for Fundamental Physics for support.

*Ruth.Bamford@stfc.ac.uk
Also at York Plasma Institute, Department of Physics, University of York, Heslington, York, YO10 5DD, United Kingdom.
†Also at Central Laser Facility, Rutherford Appleton Laboratory, Chilton, Didcot, OX11 0QX, United Kingdom.

[1] R. P. Lin, D. L. Mitchell, D. W. Curtis, K. A. Anderson, C. W. Carlson, J. McFadden, M. H. Acuna, L. L. Hood, and A. Binder, Science **281**, 1480 (1998).
[2] G. Y. Kramer *et al.*, J. Geophys. Res. **116**, E00G18 (2011).
[3] C. F. Kennel and R. Z. Sagdeev, J. Geophys. Res. **72**, 3303 (1967).
[4] D. McKay, G. Heiken, A. Basu, G. Blanford, S. Simon, R. Reedy, B. M. French, and J. Papike, in *The Lunar Sourcebook*, edited by G. Heiken, D. T. Vaniman, and B. M. French (Cambridge University Press, Cambridge, England, 1991), p. 736.
[5] I. Garrick-Bethell *et al.*, Icarus **212**, 480 (2011).
[6] A. B. Binder, Science **281**, 1475 (1998).
[7] M. Kato, S. Sasaki, Y. Takizawa, and the Kaguya Project Team, Space Sci. Rev. **154**, 3 (2010).
[8] J. N. Goswami and M. Annadurai, Acta Astronaut. **63**, 1215 (2008).
[9] N. Ichiro, J. Space Technol. Sci. **19**, 1 (2003).
[10] J. S. Halekas, D. A. Brain, R. P. Lin, and D. L. Mitchell, Adv. Space Res. **41**, 1319 (2008).
[11] M. Wieser *et al.*, Geophys. Res. Lett. **37**, L05103 (2010).
[12] K. Hashimoto *et al.*, Geophys. Res. Lett. **37**, L19204 (2010).
[13] Y. Saito *et al.*, Geophys. Res. Lett. **35**, L24205 (2008).
[14] Y. Saito, S. Yokota, T. Tanaka, K. Asamura, M. Nishino, T. Yamamoto, K. Uemura, H. Tsunakawa, and the Kaguya Map Team, Geophys. Res. Abs. **12**, 6000 (2010).
[15] Y. Futaana, S. Barabash, M. Wieser, M. Holmström, A. Bhardwaj, M. B. Dhanya, R. Sridharan, P. Wurz, A. Schaufelberger, and K. Asamura, J. Geophys. Res. **115**, A10248 (2010).
[16] Y. Futaana, S. Machida, Y. Saito, A. Matsuoka, and H. Hayakawa, J. Geophys. Res. **108**, 1025 (2003).
[17] M. Wieser, S. Barabash, Y. Futaana, M. Holmström, A. Bhardwaj, R. Sridharan, M. B. Dhanya, P. Wurz, A. Schaufelberger, and K. Asamura, Planet. Space Sci. **57**, 2132 (2009).
[18] A. D. R. Phelps, Planet. Space Sci. **21**, 1497 (1973).
[19] L. C. Woods, *Principles of Magnetoplasmas* (Clarendon, Oxford, 1987), p. 397.
[20] D. Tidman and N. A. Krall, *Shock Waves in Collisionless Plasmas*, edited by S. C. Brown (John Wiley & Sons, New York, 1971).
[21] R. Bingham, *Plasma Physics: An Introductory Course*, edited by R. Dendy (Cambridge University Press, Cambridge, England, 1993).
[22] J. B. McBride, E. Ott, J. Boris, and J. H. Orens, Phys. Fluids **15**, 2367 (1972).
[23] R. Bingham, R. Bamford, B. J. Kellett, and V. D. Shapiro, J. Plasma Phys. **76**, 915 (2010).
[24] C. Lue, Y. Futaana, S. Barabash, M. Wieser, M. Holmström, A. Bhardwaj, M. B. Dhanya, and P. Wurz, Geophys. Res. Lett. **38**, L03202 (2011).
[25] M. G. Rusbridge, G. Sewell, H. Qaosim, D. A. Forder, M. Kay, A. Randewich, A. Mirarefin, P. K. Browning, K. J. Gibson, and J. Hugill, Plasma Phys. Controlled Fusion **42**, 579 (2000).
[26] R. A. Bamford *et al.*, Plasma Phys. Controlled Fusion **50**, 124025 (2008).